Granular Matter

Coupled CFD-DEM method for consolidated un-drained tri-axial test of methane hydrate bearing sediments

--Manuscript Draft--

Manuscript Number:	
Full Title:	Coupled CFD-DEM method for consolidated un-drained tri-axial test of methane hydrate bearing sediments
Article Type:	Original Report
Keywords:	methane hydrate bearing sediments; consolidated drained; coupled CFD-DEM method
Corresponding Author:	Mingjing Jiang, Ph.D Tongji University Shanghai, CHINA
Corresponding Author Secondary Information:	
Corresponding Author's Institution:	Tongji University
Corresponding Author's Secondary Institution:	
First Author:	Mingjing Jiang, Ph.D
First Author Secondary Information:	
Order of Authors:	Mingjing Jiang, Ph.D
	Wei Zhou
	Marcos Arroyo
	Wang Cheng Zhang
Order of Authors Secondary Information:	
Funding Information:	the EU FP7IRSES “Geohazards and Geomechanics” (No. 294976) — Professor Mingjing Jiang
	the Program for Changjiang Scholars and Innovative Research Teamin University of China (No. IRT1029) — Professor Mingjing Jiang
	he Research Fund of the Doctoral Program of Higher Education (No. 20100072110048) — Professor Mingjing Jiang
	National Science Foundation of China for Distinguished Young Scientists (No. 51025932) — Professor Mingjing Jiang
	the Major Project of Chinese National Program for Fundamental Research and Development (973Program) (No. 2011CB013500) — Professor Mingjing Jiang
Abstract:	Abstract: Methane hydrate (MH), a potential source of future energy, is extensively deposited in marine deposits. It is essential to understand the mechanical properties of methane hydrate bearing sediments (MHBS) for applications relevant to mining and geotechnical engineering. This study aims to investigate the undrained shear strength of methane hydrate bearing sands. The current paper presents a coupled Computational Fluid Dynamics and Discrete Element Method (CFD-DEM) numerical approach to simulate the behavior of fluid-particle interaction system. The Tait equation of state for liquid is implemented into the Navier-Stokes equation-based CFD, while the DEM is used to model the granular particle system of MH bearing sediments. The validity of the CFD-DEM tool is first verified by two typical geomechanics problems where analytical solutions are available. The simulations show that the stress-strain

	behaviors of MHBS emerge the temperature, pore pressure and saturation degree dependency, the curves shows a softening-like response, the shear mechanical property including the peak deviator stress and frictional angle increase with the increase of initial pore pressure and MH saturation as well as the decrease of temperature.
Suggested Reviewers:	

Title: Coupled CFD-DEM method for consolidated un-drained tri-axial test of methane hydrate bearing sediments

Mingjing Jiang[1, 2, 3*], Wei Zhou[1, 2, 3], Marcos Arroyo[4], Wangcheng Zhang[1, 2, 3]

[1] *State Key Laboratory for Disaster Reduction in Civil Engineering, Tongji University, Shanghai, China, 200092*

[2] *Key Laboratory of Geotechnical and Underground Engineering of Ministry of Education, Tongji University, Shanghai, China, 200092*

[3] *Department of Geotechnical Engineering, College of Civil Engineering, Tongji University, Shanghai, China, 200092*

[4] *Department of Geotechnical Engineering and Geosciences, Universitat Politècnica de Catalunya, Barcelona, Spain*

* Corresponding author: Dr. Mingjing Jiang, Professor of Geotechnical Engineering, 'Professor of Exceptional Rank in Tongji University'

Tel: +0086-21-65980238; Fax: +0086-21-65985210;

E-mail: mingjing.jiang@tongji.edu.cn

Abstract**:** Methane hydrate (MH), a potential source of future energy, is extensively deposited in marine deposits. It is essential to understand the mechanical properties of methane hydrate bearing sediments (MHBS) for applications relevant to mining and geotechnical engineering. This study aims to investigate the undrained shear strength of methane hydrate bearing sands. The current paper presents a coupled Computational Fluid Dynamics and Discrete Element Method (CFD-DEM) numerical approach to simulate the behavior of fluid-particle interaction system. The Tait equation of state for liquid is implemented into the Navier-Stokes equation-based CFD, while the DEM is used to model the granular particle system of MH bearing sediments. The validity of the CFD-DEM tool is first verified by two typical geomechanics problems where analytical solutions are available. The simulations show that the stress-strain behaviors of MHBS emerge the temperature, pore pressure and saturation degree dependency, the curves shows a softening-like response, the shear mechanical property including the peak deviator stress and frictional angle increase with the increase of initial pore pressure and MH saturation as well as the decrease of temperature.

Key words*: methane hydrate bearing sediments; consolidated drained; coupled CFD-DEM method*

1 Introduction

Methane hydrates are crystalline clathrates composed of water and methane molecules under specific temperature and pressure conditions. Being considered to be one of the potential energy resources to alleviate the energy crisis, the presence of methane hydrate is commonly found worldwide deposited in continental marine sediments, forming the methane hydrate bearing sediment. The extraction of methane hydrate has attracted interests of many investigators in many countries including the United States, China, Russia and India among others. However, the presence of methane hydrate also bring some challenges to geotechnical engineers, this is because the dissociation of methane hydrate can not only result in a loss of cementation but also an increase of excess pore pressure of methane hydrate grounds, which in turn can cause a degradation of methane hydrate grounds and corresponding geo-hazards like ground destabilization, submarine landslides and platform destructions. So it is essential to access the mechanical properties especially the shear strength characteristics for applications relevant to mining and geotechnical engineering.

To date, some understanding of MHBS mechanical properties has been acquired via tests on natural and artificial specimens [1-5]**.** Most of the existing data is based on consolidated-drained (CD) tests, the mechanical response under drained conditions has been extensively studied by means of numerical analysis and experiments considering many factors like temperature, effective pressure, saturation degree of methane hydrate as well as time dependency. Fewer studies have been conducted using consolidated un-drained (CU) tests. However, the relative low permeability of some MHBS suggests that parameters from CU tests may be relevant in many practical situations. So there exists strong necessity to acquire the CU values before construction of practical MH-related engineering projects.

Researchers [6] have performed laboratory tests to directly determine the CU strength values of methane hydrate bearing sediments using the triaxial apparatus. However, such testing is quite complicated and time-consuming due to the high pressure and low temperature requirements, as well as poor repeatability in specimen formation. Numerical methods, especially Discrete Element Method offers one alternative approach to explore that behavior, particularly if it involves the coupling effect of particle-fluid interaction in addition to particle-particle interactions. The so-called combined approach of Discrete Element Method and Computational Fluid Dynamics (CFD-DEM) has been developed [7-9] and proved to be effective [10-18] in modeling geomechnical problems like seismic liquefaction, seepage of soil slope and other mechanical problems like fluidization, cyclone, and film coating (summaried by [19]). To the authors' knowledge, few studies have been made on the particle-fluid flow system for MHBS CU triaxial tests by means of CFD-DEM approach.

The current paper aims to develop a coupled CFD-DEM numerical tool to determine the CU strength characteristics of MHBS. Firstly, the governing equations in consideration of proper interaction force exchanges between the DEM and the CFD are introduced including equations for fluid-particle interaction forces, Navier-Stokes equation for the fluid-flow, Tait equation of state for fluid and motion equations for particle system. The proposed CFD-DEM model is then validated by two benchmarking examples, namely, the single particle free settling problem and the one-dimensional consolidation problem. At last, numerical simulation results of MHBS under CU conditions with a specific temperature, back pressure and MH saturation degree presented, the effect of these three strength factors are then studied before coming to the conclusions.

2 Methodology and formulations

2.1 Governing equations for the pore fluid and particle system

In the CFD method, the fluid is treated as a continuum and the geometry domain is discretized into a certain number of computational cells for calculation efficiency. In CFD-DEM the fluid only occupies the porous fraction (*n*) of the material. Local averaging within the pore space of each cell of variables such as fluid velocity, pressure and density is assumed possible. Therefore for each cell the continuity and the conservation of momentum equations are written as:

$$\frac{\partial(n\rho_f)}{\partial t}+\nabla(n\rho_f\cdot U^f)=0 \tag{1}$$

$$\frac{\partial(n\rho_f U^f)}{\partial t}+\nabla\cdot(n\rho_f U^f U^f)+F^f-n\nabla\cdot(\mu\nabla U^f)=-\nabla P+n\rho_f g \tag{2}$$

Where n is the local void fraction defined as: $n=V_{void}/V_c$, (V_c is the total volume of a cell, v_{void} is the total cell volume minus the volume of the particles in the cell) ; U^f is the average velocity of the fluid in the cell; P is the averaged pore pressure in the cell; ρ_f is the averaged fluid density; μ is the averaged viscosity; g is the gravitational acceleration; F^f is the particle-fluid interaction force average of that exerted on the fluid by particles inside the cell.

By observing *eq*. 2, the pore pressure (P) not only varies with the fluid-flow (associated with left terms of *eq*. 2) but also with the density (ρ_f) variation of the fluid. Assuming that MHBS would be saturated with seawater, fluid density variation can be described by the equation of state proposed by [20] given as:

$$\frac{\rho_f - \rho_{f0}}{\rho_{f0}} = 0.315 \cdot (1 - S \times 10^{-3}) \cdot \log\left(\frac{B^* + P}{B^* + P_0}\right) \tag{3}$$

Where B* (unit of B^* is in *bar*, 1 *bar*=10^5 Pa) is fitting parameters for seawater respectively based on laboratory tests which can be given by:

$$B^* = (2670 + 6.89656 \times S) + (19.39 - 0.0703178 \times S)t - 0.223t^2 \tag{4}$$

Where ρ_{f0}/P_0 and ρ_f/P are initial density/pressure and current density/pressure of fluid, respectively; S is salt concentration of seawater; t is temperature of water (unit in℃)

For a given particle p in DEM, the following equations govern its translational and rotational motions:

$$m_p \frac{du_p}{dt} = m_p g + \sum_{i=1}^{n_p} (F_{pi}^c + F_{pi}^d) + F_p^f \tag{5}$$

$$I_p \frac{d\omega_p}{dt} = \sum_{i=1}^{n_p} M_p \tag{6}$$

Where m_p, u_p, ω are the mass, velocity and rotational velocity of the single particle p, respectively; F_p^c, F_p^d, F_p^f are contact force, viscous damping force and particle-fluid interaction force which includes both pressure gradient force and drag force in the current case acting on particle p; M_{pi} are the contact force and the torque acting on particle p by particle i or the wall(s); n_p is the number of total contacts for particle; I_p is moment of inertia of particle p. m_pg is the gravitational force.

In the DEM code, as shown in Fig. 1, Jiang et al. [21,22] proposed a cemented contact model for MHBS in conjunction with Coulomb's friction laws shown in Fig. 2(a)-(c) to describe the inter-particle contact mechanical behavior. This contact model of MHBS relates the microscopic bond strengths given in *eq*. (7) with macroscopic quantities of MH's environmental conditions (i.e., Pore water pressure, temperature and MH saturation degree) by *eq*s. (8)-(11), more details can be seen in [22]. Interested readers should note that *eq*s. (10)-(13) are fitting equations based on pure MH compression tests conducted by Hyodo et al. [1] at certain temperature and pore pressure conditions (i.e., temperature from -30℃ to 5℃ and pore pressure from 1.5 to 20MPa). Since MHs are usually formed at 100 to 2000 m below the sea level, equivalent to an initial pore pressure from 1MPa to 20MPa, these equations are relevant for DEM simulations under temperature and pore pressure conditions listed in Tab. 1.

$$R_s = f_s \cdot K_s{}^p \cdot (F_n{}^p + R_{tb})(\ln \frac{R_{cb} + R_{tb}}{F_n + R_{tb}})^{0.59} \tag{7a}$$

$$R_r = f_r \cdot K_r{}^p \cdot (F_n{}^p + R_{tb})(\ln \frac{R_{cb} + R_{tb}}{F_n + R_{tb}})^{0.59} \tag{7b}$$

$$R_{\mathrm{tb}} = \mathrm{B}\ q_{t,max} \tag{7c}$$

$$R_{\mathrm{cb}} = \mathrm{B}\ q_{c,max} \tag{7d}$$

Where R_s is bond shear resistance, R_r is bond rolling resistance and R_{tb}/R_{cb} are bond tension/compression resistance; K_s^p, K_r^p are normal, tangential, and rolling stiffness; f_s, f_r are fitting parameters associated with the minimum bond thickness (h_{min}), $q_{t,max}$ and $q_{c,max}$ are the tensile and compressive strength of pure MHs, F_n^p is the normal contact force, which can be respectively formulated based in in-situ experiments [1] as follows:

$$\begin{cases} f_s = 2.05 - 0.89e^{-(1000h_{\min} - 1.15)^2} \\ K_s^{\ p} = 0.41 - 61.07h_{\min} \\ f_r = 2.05 - 0.92e^{-(1000h_{\min} - 1.15)^2} \\ K_r^{\ p} = 0.83 - 146.36h_{\min} \end{cases} \tag{8}$$

$$\begin{cases} \dfrac{q_{t,\max}}{p_a} = 0.45\left(\dfrac{p_c}{p_a}\right) - 1.15\left(\dfrac{T}{T_0}\right) + 101.75\left(\dfrac{\rho}{\rho_w}\right) - 74.39 \\ \dfrac{q_{c,\max}}{p_a} = 0.81\left(\dfrac{p_c}{p_a}\right) - 2.08\left(\dfrac{T}{T_0}\right) + 184.16\left(\dfrac{\rho}{\rho_w}\right) - 134.65 \end{cases} \tag{9}$$

$$\begin{cases} F_n^{\ p} = \begin{cases} K_n^{\ p} \cdot u_n, & u_n \geq \ \ 0 \\ 0, & u_n < 0 \end{cases}, \\ \dfrac{E}{p_a} = 3\left(\dfrac{p_c}{p_a}\right) - 1.98\left(\dfrac{T}{T_0}\right) + 4950.50\left(\dfrac{\rho}{\rho_w}\right) - 1821.78 \end{cases} . \tag{10}$$

Where K_n^p is the normal stiffness; u_n is the overlap of contacted particles; ρ is the density of pure MHs under a confining pressure (p_c) and the temperature (T); p_a is the standard atmospheric pressure (i.e., 1.01×10^5Pa); T_0 is the reference temperature of 1 ℃; and ρ_w is the density of water at 4 ℃. Note that p_c is equal to the pore water pressure for MH bonds in submerged specimens of MHBS. h_{min} and B are geometrical quantities derived from the saturation degree of MH (S_{Hb}); $S_{Hb} = V_{MH}/V_V \cdot 100\%$, defined as the ratio of the area of voids occupied by MH bonds to the total void area.

$$S_{Hb} = \frac{1+e_p}{e_p A}\sum_{i=1}^{m}\left(h_{\max}^{cr} B_i - 2\bar{R}_i^2 \arctan\frac{B_i}{\sqrt{4R_i^2 - B_i^2}} + B_i\sqrt{R_i^2 - \left(\frac{B_i}{2}\right)^2}\right) + S_{H0} \tag{11}$$

Where A is the total cross section of the specimen; e_p is the planar void ratio (i.e., the ratio of total void area against the area of soil particles in two dimensions). S_{H0} is the threshold MH saturation at which MH begins to cement sandy grains depending on the deposition history [23,24]. m is the total number of MH bonds. The status of the bond (i.e., intact or broken) for a particle p is determined through a bond failure criterion arising from micromechanical tests on idealized bonded granules [25,26]. This criterion shown in Fig. 2(d) in general can be written as:

$$\frac{F_s^{p2}}{R_s^2}+\frac{M^p}{R_r^2}=\begin{cases}\geq 1, & \text{intact bond}\\ <1, & \text{broken bond}\end{cases} \tag{12}$$

2.2 Fluid-particle interaction forces

The key to model a particle-fluid coupling system is to take the particle-fluid interaction forces into consideration in addition to particle-particle interaction forces in DEM and fluid-fluid interaction forces in CFD. Particle-fluid interaction forces include hydrostatic buoyancy, pressure gradient force, and other hydrodynamic forces like the drag force, virtual mass force, basset force and lift forces (see in [19]). In this study, we consider that the dominant interactions between fluid and submerged particles of MHBS in CU triaxial tests are those due to pressure gradient and drag. The expression employed to compute the force due to fluid pressure gradient on the particles is:

$$\begin{cases} f_i=-\dfrac{\partial p}{\partial y}\displaystyle\sum_{m=1}^{n_p}V_p^m=-(1-n)\dot{P}_{,i}\\ V_p^m=\dfrac{\pi}{6}d_{pm}^3\end{cases} \tag{13}$$

Where p, n_p is the averaged water pressure and particle number within a cell; and n is porosity; V_p^m is volume of a specific particle m with a diameter of d_{pm}.

To date, there are no analytical solutions to calculate the drag force for a cluster assembly of submerged particles within a cell. We follow the empirical equations proposed by Ergun [27] and Wen et al. [28] associated with the void ratio of the cell (n):

$$\begin{cases} f_i = (1-n)(150\dfrac{\mu(1-n)}{n\bar{d}_p^2} + 1.75\dfrac{\rho_f\,|u_i - \bar{u}_i|}{\bar{d}_p})(u_i - \bar{u}_i),\ (n<0.8) \\ f_i = 0.75(1-n)\dfrac{C_D R_e n^{-2.65}\mu\rho_f\,|u_i - \bar{u}_i|}{\bar{d}_p}(u_i - \bar{u}_i), (n > 0.8) \end{cases} \tag{14}$$

Where u_i / $\bar{u}_i$ are flow velocities/horizontal component vertical component, i=1,2; $\bar{d}_p$ is average diameter of particles in a cell; μ is dynamic viscosity; R_e is Reynolds number which can be expressed by:

$$R_e = n\rho_f \bar{d}_p |\mathbf{u}_f - \bar{\mathbf{u}}_p| / \mu \tag{15}$$

Where $\mathbf{u}_f$, $\bar{\mathbf{u}}_p$ are average velocity of fluid and particle of a cell, respectively; the drag force coefficient (C_D) in *eq*.(14) can be formulated by:

$$C_D = \begin{cases} \dfrac{24}{R_e}(1+0.15R_e^{0.687}), & R_e \le 1000 \\ 0.44 & R_e \ge 1000 \end{cases} \tag{16}$$

2.3 Numerical solution schemes for coupled CFD-DEM computation

Though the mathematic model for CFD-DEM computation is complicated, the theory of numerical coupling method is simple. The fluid phase is discretized with fixed sized cells, these cells are used to determine which cell does an individual particle belongs to. Fig. 3 shows the general algorithm of coupled DEM-CFD simulations. Firstly, by following the coarse-grid approximation method proposed by Tsuji et al. [29], CFD program is used to solve the locally-averaged Navier-Stokes equation in *eq*. (2) for the averaged velocity and pressure for each cell, this information is then passed to the coupling module. By using the position and velocity provided by DEM modules, the relative velocity between each particle and the surrounding fluid is acquired and the pressure gradient force and drag force can be obtained by *eq*s. (13)-(14), then DEM solver updates the positions by *eq*s. (5)-(6) in a loop until the end of the CFD time step is reached. The particles new position information is handed back to the coupling module which will update the new fluid cell porosities. Based on these steps, the CFD solver iterates over the time until the flow field converges to a stable solution.

3 Benchmarking examples

In order to validate the CFD-DEM tools proposed for testing the CU strength of MHBS in this current paper, two coupled calculation problems with available analytical solutions are implemented, namely single spherical particle free settling in the water and one dimensional consolidation problem.

3.1 Single spherical particle free settling in the water

Stokes analytically found that a spherical particle settles in water with a uniform terminal velocity due to the balance of buoyance and drag force with the gravitational force as:

$$\underbrace{\frac{\pi}{6} d_p^3 (\rho_p - \rho_f) g}_{gravity\ force - buoyance\ force} = \underbrace{C_d R_e \mu \frac{\pi}{4} d_p^2 \rho_f \frac{v_y^2}{2}}_{drag\ force} \tag{17}$$

Where v_y is the particle terminal sedimentation velocity. By solving *eq*. (17), v_y can be further formulated by:

$$v_y = \sqrt{\frac{4(\rho_p - \rho_f) d_p g}{3 C_d R_e \mu \rho_f}} \tag{18}$$

Fig. 4 (see inset of Fig. 4) presents the coupled CFD-DEM simulation model of a spherical particle of d_p=1mm is dropped freely from the center of water surface in a container with a L×H=420×840mm calculated in the plane-strain condition with an out-of-plane thickness of 1 m, the planar container was divided into 14×28 homogeneous fluid cells. The densities of the particle and the water are ρ_p=2650kg/m^3 and ρ_f=1000kg/m^3, respectively. The viscosity of water is μ=2×10^{-3}Pa·s.

Fig. 4(a) shows the simulated velocity of the dropped particle, the velocity starts from 0 m/s, presents a nonlinear increase versus the time and reaches a terminal velocity of 0.321 m/s at about 0.4s which agrees very well with the analytical solution. In conjunction with Fig. 4(b), the velocity shows a strong interplay with the drag force which increases with the increase of the particle velocity and reaches the maximum value at about 0.4s and at this moment the particle reaches a state of dynamic equilibrium (resultant force equals to gravity minus buoyant force).

3.2 One dimensional consolidation

The CFD-DEM coupled method has also been validated in another classic geo-mechanical problem of one-dimensional consolidation problem. Terzaghi [30] obtained an analytical solution to the dissipation of the excess pore water (u_w) in an one-way drained soil layer subjected to uniform surcharge. The governing equation is given by:

$$\frac{\partial u_w}{\partial t} = C_v \frac{\partial^2 u_w}{\partial z^2} \tag{19}$$

Where t is consolidation time; z is depth of the soil; C_v is the coefficient of consolidation and can be formulated by:

$$C_v = \frac{k}{m_v \gamma_w} = \frac{k(1+e_0)}{\alpha \gamma_w} \quad (20)$$

Where k is the coefficient of the permeability, e_0 is the initial void ratio of the soil, α is the coefficient of the compressibility, γ_w is specific weight of the water, m_v is the coefficient of volume change defined as: $m_v = \Delta\varepsilon_v / \Delta\sigma_v$ ($\Delta\varepsilon_v$ and $\Delta\sigma_v$ are the variations of vertical strain and vertical stress, respectively). In addition, a non-dimensional time can be defined to conveniently describe the normalized time process:

$$T_v = \frac{C_v t}{H^2} \quad (21)$$

Where H is the length of the longest drainage path equals to thickness of soil layer in which free drainage can only take place at one boundary surface. In case of one-way drainage, the initial and boundary conditions are:

$$u(z,0) = p_0,\ u(0,t) = 0,\ \left.\frac{\partial u}{\partial t}\right|_{z=H} = 0 \quad (22)$$

Where p_0 is the uniform surcharge applied on the soil surface; taking *eq*. (22) into *eq*. (20), and the excess pore water pressure can be obtained:

$$u_w = \sum_{m=1}^{m\to\infty} \frac{2p_0}{m\pi}(1-\cos m\pi)\sin\frac{m\pi z}{2H}\exp(-\frac{m^2\pi^2 T_v}{4}) \quad (23)$$

Where m denotes an integer number.

Therefore, the average degree of consolidation (i.e. U) for soil can be expressed as:

$$U = 1 - \frac{\int_0^H u_w \mathrm{dz}}{\int_0^H \sigma \mathrm{dz}} \quad (24)$$

Substituting *eq*. (23) into *eq*. (19) the following expression can be obtained:

$$U = 1 - \frac{8}{\pi^2}\left[\exp(-\frac{\pi^2 T_v}{4}) + \frac{1}{9}\exp(-\frac{9}{4}\pi^2 T_v + \cdots)\right] \quad (25)$$

Fig. 5 shows the simulated one-dimensional consolidation problem, a total of 200 submerged particles of uniform radius r_d=1mm are used, the planar container was divided into 1×50 homogeneous fluid cells with a width of 2mm each. The excess pore pressure is only allowed to dissipate in one-way vertically by setting the top surface a drained boundary condition while keep the other three surfaces undrained and normally constrained conditions. The particle density ρ_p=2650kg/m^3, fluid viscosity μ=2×10^{-3}Pa.s, g=9.81m/s^2. Particle contact forces are described by the rolling resistance model proposed by Jiang et al. [31] and the normal/shear contact stiffness is assumed to be k_n/k_s=6*10^7/4*10^{7}N/m, the inter particle frictional/rotational coefficient is assumed to be the same of 0.5. The submerged particles are initially consolidated to a stable state under the gravitational and buoyancy forces. Afterwards, an instant surcharge load p_0=1kPa is applied by assigning concentrated forces at the top row particles of the column.

Fig. 5 shows the settlement of the top particle versus the additional pressure, as can be seen, the settlement increases linearly with the additional pressure, the coefficient of compressibility (α) is then:

$$\alpha = \frac{-\Delta e}{\Delta p} = \frac{\Delta s}{H\Delta p}(1+e_0) = 6.36\times 10^{-8}\,Pa^{-1} \tag{26}$$

By the approach proposed by Mccabe et al. [32], the coefficient of the permeability (k) can be formulated by:

$$k = \frac{g_c \psi_s{}^2 d_p{}^2 n^3 r_w}{150\mu(1-\mathrm{n})^2} \tag{27}$$

Where, g_c is the gravity scaling factor (g_c=1 under a standard gravitational field); ψ is a parameter reflecting the irregularity of the particle shape (ψ=1 when the particles are circular); n is the planar void ratio, d_p is the average grain diameter of particles, μ is the fluid viscosity, r_w is the volume weight of fluid. A value of k=0.655m/s is here obtained. Using the parameter k in *eq*s. (26)-(27), the normalized analytical solution is obtained. As shown in Fig. (6)-(7), the predicted dissipations of excess pore pressure and the predicted degree of consolidation are in good agreement with the analytical solutions although small differences with numerical solutions also emerge. The precision will be improved if the particle size become smaller to the fluid cell.(see in [33])

The above two benchmarking examples illustrated the CFD-DEM program adopted in this study can reasonably capture the fluid-particle interaction, the numerical results acquired are found satisfactory with theoretical solutions and can be reliably used in associated geotechnical engineering problems.

4 Simulation program for MHBS

Tab. 1 summaries the simulation program to define the effect on strength parameters of the discrete analogue of MHBS of three typical strength-affecting factors, namely, the temperature (T), the saturation degree of MH (S_{Hb}) and initial pore pressure (*P. P*). Results for a clean sandy soil with S_{Hb}=0% are also presented here for comparison. To define shear strength at each condition specimens were tested under effective pressures (σ_3) of 1MPa, 2MPa and 3MPa. A total of 30 different numerical tests were thus performed in this study. Since there is no available direct laboratory test results to compare with numerical results, the discrete MHBS is first benchmarked under a specific condition (i.e., T=268K, P=10MPa, S_{Hb}=25%), and then the testing conditions are varied to observe the temperature, back pressure and saturation degree effects. Clearly, to perform an undrained test in the lab at those reference conditions the freezing point should be depressed below that of typical seawater, e.g. by raising salt concentration in the water.

5 Simulation procedures for CU tests

5.1 Sample preparation

The sample chosen for the analyses (Fig. 8) has enough resolution while maintaining computational efficiency. It has 400mm in width and 800 mm in height, and contains a total number of 6,000 particles. Fig. 9 shows the particle-size distribution adopted in this study with a median particle diameter (d_{50}) of 7.6 mm and the uniformity coefficient (C_u) of 1.3. Tab. 2 lists the values of parameters adopted in the simulations. The multilayer under-compaction method (UCM) proposed by Jiang et al. [34] was implemented to generate an initial homogenous sample. Five layers of particles were then generated in sequence, with each layer consisting of 1,200 particles randomly distributed into the rectangular container. To obtain an initial planar void ratio of 0.22, the accumulated layers of particles were compacted to an intermediate void ratio which is slightly higher than the target one. Based on the under-compaction criterion [34], the intermediate void ratios for the accumulated layers were $e_{\mathrm{p}(1)}$ =0.27, $e_{\mathrm{p}(1-2)}$ =0.269,$e_{\mathrm{p}(1-3)}$ =0.265, $e_{\mathrm{p}(1-4)}$ =0.259, $e_{\mathrm{p}(1-5)}$ =0.25. During each compaction process, the top wall was moved downward at a constant velocity of 0.5 m/% while the lateral and the bottom walls were fixed. The inter-particle friction coefficient was set to 1.0 in order to achieve the relatively high intermediate void ratio. During the process of sample generation, the wall–particle friction was set to zero to eliminate any boundary effects.

5.2 Bond activation

After specimen generation, the inter-particle friction coefficient was set to 0.5 and samples were consolidated one-dimensionally under a constant pressure of 200kPa. Bonds were then activated at the contacts where the inter-particle separation (i.e., t_0 in Fig. 1) was less than a threshold, arbitrarily selected as 5% of the average particle diameter in this study. The bonding strength parameters associated with MH bonds were computed in this phase according to the test conditions (i.e., effective confining pressure, back pressure, temperature and MH saturation degree) given in *eq*s. (7)-(10). For the clean sandy sand, no bonds were activated.

5.3 Isotropic consolidation

The stress controlled rigid boundary was implemented in the code using servo system. This sample was then isotropically subjected to a target confining pressure (i.e., 1MPa, 2MPa, 3MPa).

5.4 Biaxial undrained compression

After the consolidation of a specific confining pressure, the sample was compressed by moving the top and the bottom platens towards each other at a constant strain rate of

0.5% per minute while maintaining constant pressure on the lateral boundaries. In order to keep the compatibility conditions, a velocity-loading boundary condition at an equal rate of 0.5% per minute of the fluid was also implemented on the top and bottom boundary and no flow is allowed through the lateral boundary. At this stage, the pressure acting on the servo system wall is the total pressure including the pore pressure. The membrane particles neighbouring the walls were used to transfer concentrated forces converted by pore pressure using *eq*. 28, the magnitude of the force on a single membrane particle is applied according to its radius ratio of adjacent particles. Taking particle A and B for example, assuming a resultant force equals to F_{AB} due to the pore pressure acting against a total length equals to r_A+r_B between particle A and B, the magnitude of the concentrated force on particle A and B will calculated by :

$$F_A = F_{AB} \cdot \frac{r_A}{r_A + r_B}, \quad F_B = F_{AB} \cdot \frac{r_B}{r_A + r_B} \tag{28}$$

A typical sample after consolidation is plotted in the right panel of Fig. 8. Interested readers need to note that in the above three steps before the biaxial undrained compression the simulations use DEM without a coupling CFD calculation. Measurement circles are also used to monitor the variation of pore pressure. By this method, we extract the effective pressure (σ') by substracting the pore pressure(u) from the total pressure (σ) as:

$$\sigma' = \sigma - u \tag{29}$$

It is noted that the effective stress can also be acquired by averaging contact forces within a CFD cell. We compared this two numerical post processing methods and found a negligible discrepancy between the results of this two approaches.

6 Numerical results and discussion

In the following sections, we report the numerical results from the biaxial compression tests outlined in table 1. In the description of the state of stress, the following 2D invariant variables have been used: $p=(\sigma_1+\sigma_3)/2$ (mean effective stress) and $q=(\sigma_1-\sigma_3)/2$ (deviator stress). For brevity, based on Tab. 1, we first report the behavior of a reference MHBS sample at specified environmental conditions and then report the effect of saturation degree, temperature and back pressure on the mechanical behavior.

6.1 Stress-strain relationships of MHBS

Fig. 10(a) illustrates the stress-strain curves under different confining pressures for MHBS of T=268K and P=10MPa with a saturation degree (S_{Hb}) of 25%, the curves show a softening-like response, with maximum deviator stress near 1% axial strain and increasing with the confining pressure. Fig. 10(b) illustrates the evolution of excess pore pressure within the cells at different axial displacement stages, the magnitude of the excess pore pressure increases until about 0.75%-1% axial strain and then suffers a gradual decline until the end. The maximum excess pore pressure increases with confining pressure. Fig. 10(c) presents the total and effective stress paths during loading. Linear failure envelopes can be fitted to the peak strength to estimate internal/effective frictional angle φ/φ' as well as total cohesion/effective cohesion c/c'. Fig. 11 shows the evolution of bonding breakage with axial strain, broken bonds between particles are marked in red (compression failure) and black (tension failure). There exists a strong interplay between the bonding breakage and the evolution of shear bands, the broken bonds increase with the expansion of shear bands when the axial strain grows. When the axial displacement reaches 12%, a distinct breakthrough shear band was observed along the diagonal line of the rectangle. By comparing the stress-strain curve of the MHBS with that of the clean sandy soil, in Fig. 10(a), we found there was a coincidence of the strength value in the residual phase of the curves. This coincidence shows that at that stage the practically unbounded band dominates the response, and that while there are still some intact bonds within blocks surrounded by shear bands and several they contribute little to the deviator stress.

6.2 Effect of Temperature and back pressure

Fig. 12 and Fig. 13 present the stress-strain curves of the MHBS under different temperatures and back pressures and corresponding evolution of excess pore pressure. As shown in Fig. 12, the peak strength and the initial tangent modulus increases with the decrease of the temperature; the temperature has a small impact on the maximum excess pore pressure while it dissipates faster under a lower temperature.

As for the effect of back pressure (Fig. 13), the peak shear strength increase with the increase of pore pressure while the evolution of pore pressure presents almost the same magnitude with the axial strain development. With the same approach adopted in Fig. 10(c), the effective/total frictional angle and effective cohesion/ total cohesion versus the temperature and pore pressure is presented in Fig. 14, it was found that the frictional angle as well as the cohesion increased with the increase of back pressure and the decrease of the temperature.

6.3 Effect of Methane Hydrate Saturation

Fig. 15 presents the stress-strain relationship under different effective confining pressures and hydrate saturation (S_{Hb}) of MHBS at T=283K, P. P=10MPa.The brittle response, as well as maximum deviator stress and excess pore pressure are greatly enhanced by saturation degree. The variation of effective peak shear strength σ_{peak} with respect to the saturation degree is shown in Fig. 16, in which the relationships with different confining pressure are included. The peak shear strength increases dramatically as the effective confining pressure increases at any S_{Hb}.

Based on triaxial tests on a physical analogue of MHBS (mixtures of sand, silt, clay with Tetrahydrofuran), Santamarina and Ruppel [35] obtained an equation summarizing the effect of saturation degree on the undrained peak shear strength under different effective confining pressures as:

$$\sigma_{peak} = a\sigma_3' + bq_{\max,c}(\frac{S_{Hb}}{n})^c \tag{30}$$

Where, σ_{peak}, σ'_3 are the peak shear strength and effective confining pressure respectively; S_{Hb} is the saturation degree of MH; n is the void ratio; $q_{max,c}$ is the compression strength of pure MH which equals to 11.45MPa under the a reference temperature of 283K and a back pressure of 10MPa. *a*, *b*, and *c* are fitting parameters in which *a* captures friction and pore pressure generation in the sediment, whereas *b* gives an indication of the hydrate's ability to contribute to strength and *c* is the nonlinear effect of hydrate saturation. In their tests *c was* equal to 2, whereas a and b were dependent on sediment grain size and fabric [35].

The same equation has been fitted to the numerical results in Fig. 16. The parameters obtained (*a*=0.18, *b*=0.08 and *c*=1.15) differ from those obtained by Santamarina and Ruppel. In particular, the non-linear effect is smaller here (*c*=1.15 vs c = 2) as well as the pure friction term (*a* was above 0.5 and in the experiments). The value of b obtained here lays between those obtained in the experiments with sand (b = 0.14) and kaolinite (b=0.07). Several reasons can explain this discrepancies, like the difficulty of representing three-dimenional behavior with 2D DEM, or the fact that the Tetrahydrofuran employed in the experiments is different from the methane hydrate. Still, the qualitative agreement found is encouraging.

The data in Fig. 16 lead to a relationship of the frictional angle and cohesion versus the saturation degree in Fig. 17, as can be seen the effective/total friction angle suffered a decline from 21.1 °/16.8 ° to 17.3 °/7.36 ° when MH saturation degree transfer from 0% to 25% and then the effective/total friction angle then keeps increasing to 23 °/ 8 ° from 25% to 50%, the total/effective cohesion, the presence of MH causes a considerable increase associated with the increasing of S_{Hb} from 0MPa to almost 1.5MPa.

7 Conclusion

In this study, we employed a coupled CFD-DEM method to simulate undrained triaxial tests of MHBS. DEM was used to simulate the interactions and motion of particles by adopting a bonded contact model that explicitly accounts for the effect of ambient conditions (i.e., temperature, back pressure and saturation degree) on the clathrate bond. CFD method was used to solve the locally averaged Navier-Stokes equation for fluid flow, interaction forces between the particles and the fluid are considered by exchanging drag forces and pressure gradient force. The main conclusions of the study are summarized as follows:

(1) The proposed CFD-DEM coupled method is efficient and is capable to simulate a variety of geotechnical problems. This method was validated by two benchmark geotechnical problems, namely the single particle settling in water and the one-dimensional consolidation problem, the numerical results agree quite well with theoretical solutions.

(2) The mechanical properties of MHBS depend on the test conditions (i.e. temperature, back pressure and saturation degree). The undrained stress-strain curves of MHBS show a softening-like response, the peak strength increases with increasing effective confining pressure and the maximum deviator stress occurred in the vicinity of 1% axial strain. The strength of MHBS increases with increasing back pressure as well as decreasing temperature.

(3) The maximum deviator stress of MHBS is enhanced by MH saturation degree, the numerical undrained strength can be well adjusted using a function proposed by Santamarina and Ruppel [35].

(4) The friction angle and cohesion of methane hydrate shows a temperature, pore pressure and saturation degree dependency, the frictional angle as well as the cohesion increases with the increase of back pressure as well as the decrease of the temperature; the strength increase due to increased MH saturation causes a considerable increase in cohesion rather than friction; indeed, MHBS friction

slightly declines when the saturation degree increases from 0% to 25% and then keeps increasing until the S_{Hb} reach 50%.

On the basis of the results obtained so far the coupled DEM-CFD method seems to offer a good platform to model more challenging coupled mechanisms, such as those happening under MH dissociation conditions. In addition, a 3D calculation condition is also under consideration due to the imperfection of 2D numerical calculation in quantitative matching test results. The ultimate goal is to employ the method to numerically investigate several boundary-value problems of MHBS in geotechnical engineering, such as: wellbore instability problem and submarine landslides problem due to heating or depressurization exploitation.

Disclosures: This research was financially supported by National Science Foundation of China for Distinguished Young Scientists with Grant No. 51025932, the Major Project of Chinese National Program for Fundamental Research and Development (973Program) with Grant No. 2011CB013500, the Research Fund of the Doctoral Program of Higher Education with Grant No. 20100072110048, the EU FP7IRSES “Geohazards and Geomechanics” with Grant No. 294976, and the Program for Changjiang Scholars and Innovative Research Teamin University of China with Grant No. IRT1029. These supports are greatly appreciated.

Reference

1. Hyodo, M., Nakata, Y., Yoshimoto, N., Ebinuma, T.: Basic research on the mechanical behavior of methane hydrate-sediments mixture. Soils and Foundations **45**(1), 75-85 (2005).

2. Hyodo, M., Yoneda, J., Nakata, Y., Yoshimoto, N.: Strength and dissociation property of methane hydrate bearing sand. In: Proceedings of the 7th International Conference on Gas Hydrates (ICGH 2011), Edinburgh, Scotland, United Kingdom 2011.
3. Hyodo, M., Yoneda, J., Yoshimoto, N., Nakata, Y.: Mechanical and dissociation properties of methane hydrate-bearing sand in deep seabed. Soils and foundations **53**(2), 299-314 (2013).
4. Li, Y.-h., Song, Y.-c., Yu, F., Liu, W.-g., Zhao, J.-f.: Experimental study on mechanical properties of gas hydrate-bearing sediments using kaolin clay. China Ocean Engineering **25**, 113-122 (2011).
5. Miyazaki, K., Masui, A., Sakamoto, Y., Tenma, N., Yamaguchi, T.: Effect of confining pressure on triaxial compressive properties of artificial methane hydrate bearing sediments. In: Offshore Technology Conference 2010. Offshore Technology Conference
6. Ghiassian, H., Grozic, J.L.: Strength behavior of methane hydrate bearing sand in undrained triaxial testing. Marine and Petroleum Geology **43**, 310-319 (2013).
7. Tsuji, Y., Tanaka, T., Ishida, T.: Lagrangian numerical simulation of plug flow of cohesionless particles in a horizontal pipe. Powder technology **71**(3), 239-250 (1992).
8. Xu, B., Yu, A.: Numerical simulation of the gas-solid flow in a fluidized bed by combining discrete particle method with computational fluid dynamics. Chemical Engineering Science **52**(16), 2785-2809 (1997).
9. Zhou, Z., Kuang, S., Chu, K., Yu, A.: Discrete particle simulation of particle–fluid flow: model formulations and their applicability. Journal of Fluid Mechanics **661**, 482-510 (2010).
10. Li, Y., Zhang, J., Fan, L.-S.: Numerical simulation of gas–liquid–solid fluidization systems using a combined CFD-VOF-DPM method: bubble wake behavior. Chemical Engineering Science **54**(21), 5101-5107 (1999).
11. Xu, B., Yu, A., Chew, S., Zulli, P.: Numerical simulation of the gas–solid flow in a bed with lateral gas blasting. Powder Technology **109**(1), 13-26 (2000).

12. Rong, D., Horio, M.: Behavior of particles and bubbles around immersed tubes in a fluidized bed at high temperature and pressure: a DEM simulation. International Journal of Multiphase Flow **27**(1), 89-105 (2001).

13. Kafui, K., Thornton, C., Adams, M.: Discrete particle-continuum fluid modelling of gas–solid fluidised beds. Chemical Engineering Science **57**(13), 2395-2410 (2002).

14. Yu, A.B., Xu, B.H.: Particle‐scale modelling of gas–solid flow in fluidisation. Journal of Chemical Technology and Biotechnology **78**(2‐3), 111-121 (2003).

15. Limtrakul, S., Boonsrirat, A., Vatanatham, T.: DEM modeling and simulation of a catalytic gas–solid fluidized bed reactor: a spouted bed as a case study. Chemical Engineering Science **59**(22), 5225-5231 (2004).

16. Di Renzo, A., Di Maio, F.P.: Homogeneous and bubbling fluidization regimes in DEM–CFD simulations: hydrodynamic stability of gas and liquid fluidized beds. Chemical Engineering Science **62**(1), 116-130 (2007).

17. Tsuji, Y.: Multi-scale modeling of dense phase gas–particle flow. Chemical Engineering Science **62**(13), 3410-3418 (2007).

18. Kuang, S., Chu, K., Yu, A., Zou, Z., Feng, Y.: Computational investigation of horizontal slug flow in pneumatic conveying. Industrial & Engineering Chemistry Research **47**(2), 470-480 (2008).

19. Zhu, H., Zhou, Z., Yang, R., Yu, A.: Discrete particle simulation of particulate systems: a review of major applications and findings. Chemical Engineering Science **63**(23), 5728-5770 (2008).

20. Li, Y.H.: Equation of state of water and sea water. Journal of Geophysical Research **72**(10), 2665-2678 (1967).

21. Jiang, M., Liu, F., Zhu, F., Xiao, Y.: A Simplified Contact Model for Sandy Grains Cemented with Methane Hydrate. In: Proceedings of 18th International Conference on Soil Mechanics and Geotechnical Engineering 2013, pp. 1015-1018

22. JIANG, M.-j., Yu, X., Fang-yuan, Z.: Numerical simulation of macro-mechanical properties of deep-sea methane hydrate bearing soils by DEM. Chinese Journal of Geotechnical Engineering **35**(1), 157-163 (2013).

23. Jung, J.: Gas production from hydrate-bearing sediments: Geo-mechanical

implications. (2010).

24. Yun, T., Francisca, F., Santamarina, J., Ruppel, C.: Compressional and shear wave velocities in uncemented sediment containing gas hydrate. Geophysical Research Letters **32**(10) (2005).

25. Jiang, M., Sun, Y., Li, L., Zhu, H.: Contact behavior of idealized granules bonded in two different interparticle distances: An experimental investigation. Mechanics of Materials **55**, 1-15 (2012).

26. Jiang, M., Sun, Y., Xiao, Y.: An experimental investigation on the mechanical behavior between cemented granules. ASTM geotechnical testing journal **35**(5), 678-690 (2012).

27. Ergun, S.: Fluid flow through packed columns. Chem. Eng. Prog. **48**, 89-94 (1952).

28. Wen, C., Yu, Y.: Mechanics of fluidization. In: Chem. Eng. Prog. Symp. Ser. 2013, vol. 62, p. 100

29. Tsuji, Y., Kawaguchi, T., Tanaka, T.: Discrete particle simulation of two-dimensional fluidized bed. Powder technology **77**(1), 79-87 (1993).

30. Terzaghi, K.: Theoretical soil mechanics. (1943).

31. Jiang, M., Yu, H.-S., Harris, D.: A novel discrete model for granular material incorporating rolling resistance. Computers and Geotechnics **32**(5), 340-357 (2005).

32. McCabe, W.L., Smith, J.C., Harriott, P.: Unit operations of chemical engineering, vol. 5. McGraw-Hill New York, (1993)

33. Zhao, J., Shan, T.: Coupled CFD–DEM simulation of fluid–particle interaction in geomechanics. Powder Technology **239**, 248-258 (2013).

34. Jiang, M., Konrad, J., Leroueil, S.: An efficient technique for generating homogeneous specimens for DEM studies. Computers and geotechnics **30**(7), 579-597 (2003).

35. Santamarina, J.C., Ruppel, C.: The impact of hydrate saturation on the mechanical, electrical, and thermal properties of hydrate-bearing sand, silts, and clay. Geophysical Characterization of Gas Hydrates, Geophys. Dev. Ser **14**, 373-384 (2010).

Figure

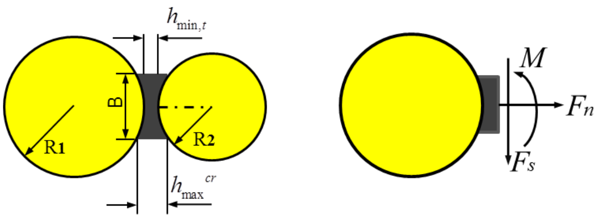

(*a*) (*b*)

Fig. 1. Schematic illustration of: (a) two sandy grains bonded by methane hydrate in between; and (b) contact forces between two particles

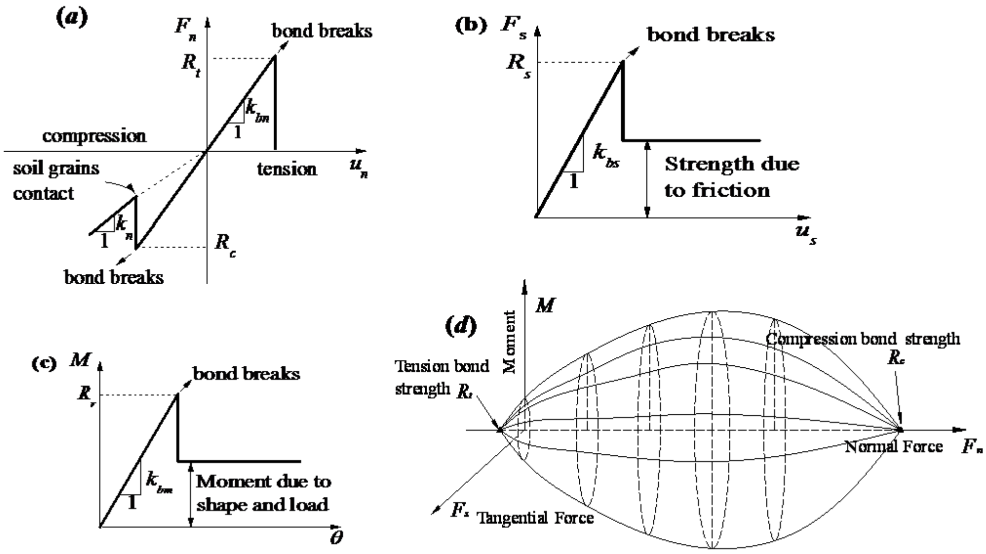

Fig. 2. Schematic illustration of a bond contact model and its mechanical response: (**a)** normal direction; (**b**) tangential direction; (**c)** rolling direction; (**d)** three-dimensional space envelope for the normal – tangential - moment strength F_n-F_s - M.

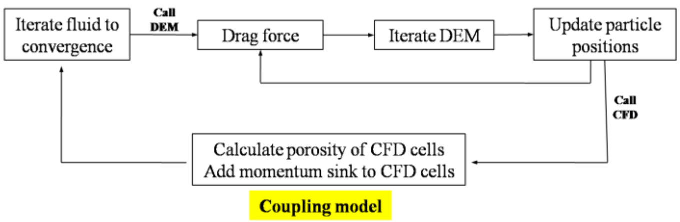

Fig. 3. Steps on coupling the motion of discrete and continuous phase (based on Favier, 2009)

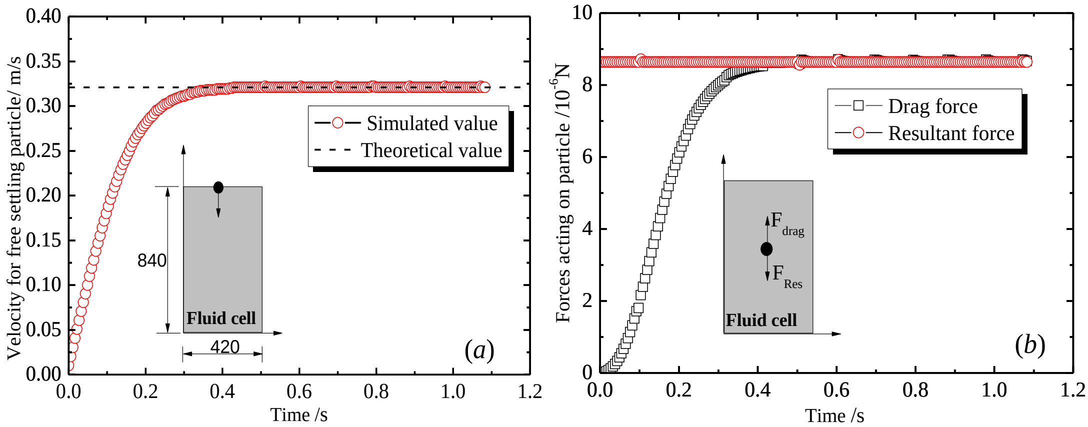

Fig. 4. Comparison of the CFD-DEM prediction and the analytical solution for single particle free settling in water: (a) Particle velocity; (b) force acting on the particle at different time

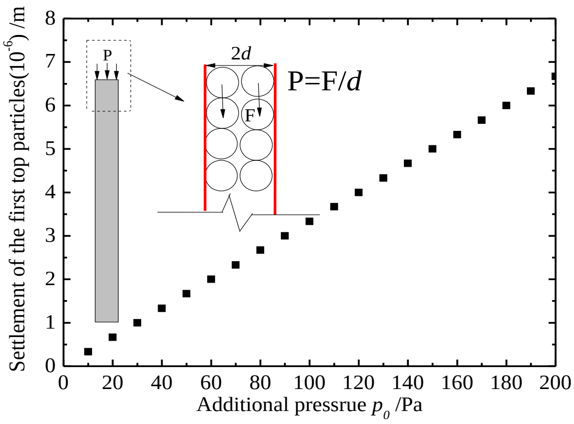

Fig. 5. Relationship between settlement of the first top particles and the additional pressure

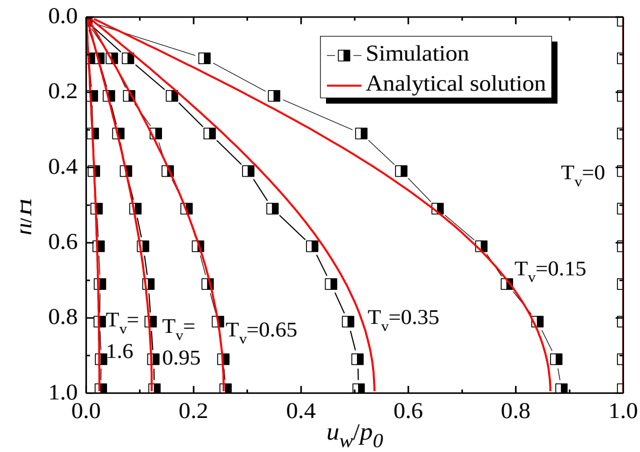

Fig. 6. Comparison of excess pore pressure between CFD-DEM numerical results and Terzaghi's theory

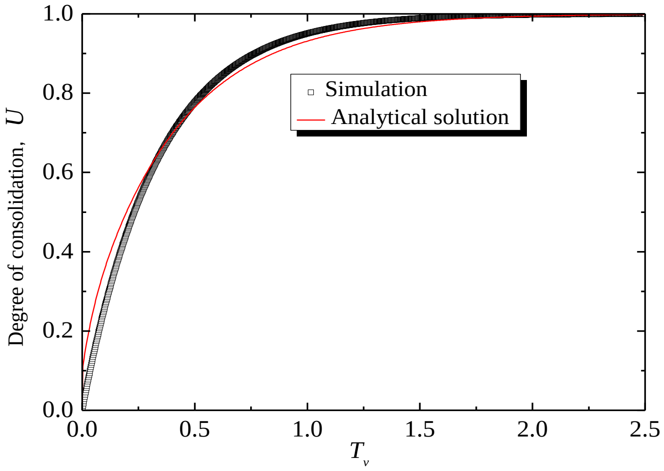

Fig. 7. Degree of consolidation with time factor in CFD-DEM simulation and Terzaghi's theory

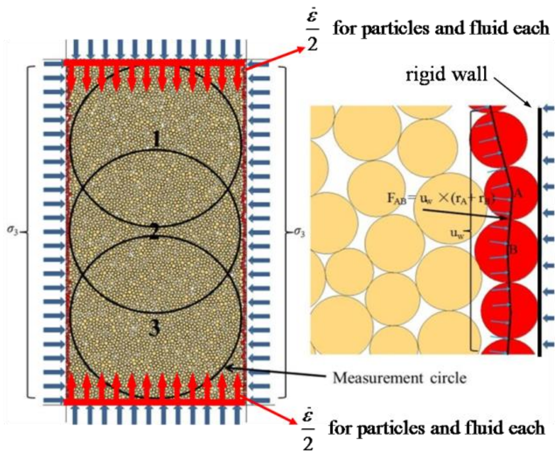

(*a*)

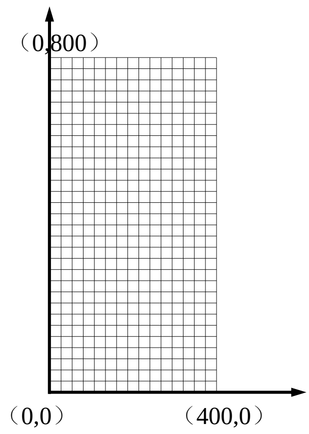

(*b*)

Fig. 8. Schematic illustration of: (*a*) The numerical sample after consolidation in DEM analyses; and (b) CFD mesh (unit in mm)

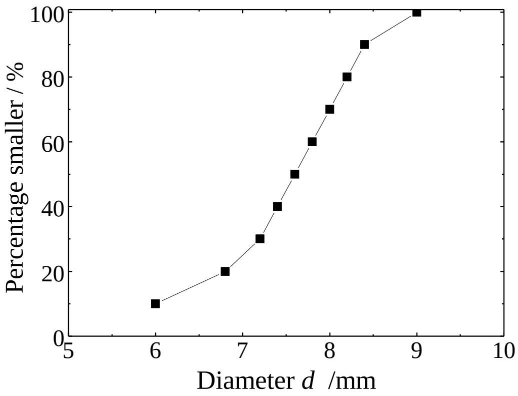

Fig. 9. Particle size distribution used in CFD-DEM simulation

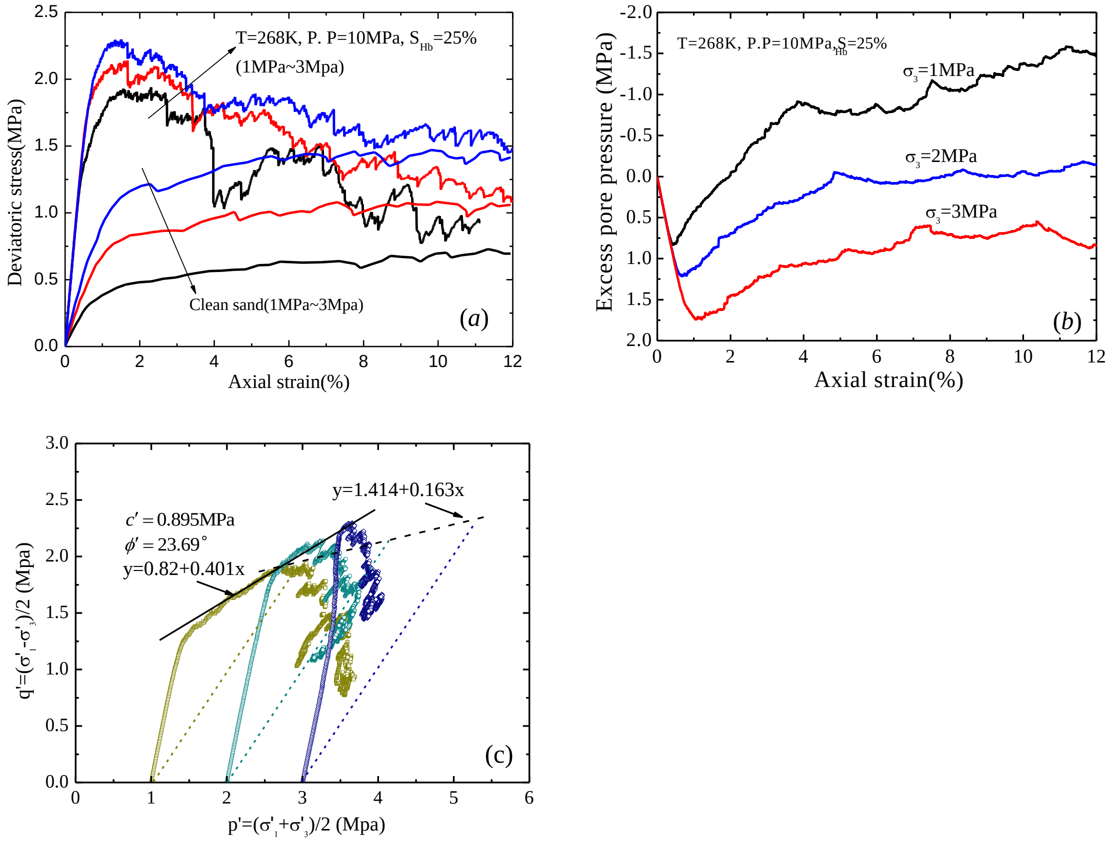

Fig. 10. (a) Stress-strain relationship and (b) corresponding evolution of excess pore pressure of MHBS at T=268K, P=10MPa and S_{Hb}=25% compared with clean sand under different effective confining pressure; (c) Effective and total envelopes for MHBS.

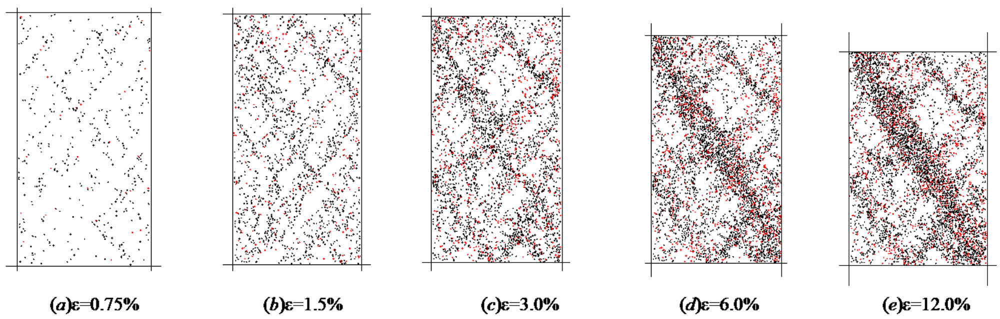

Fig. 11. Bond breakage progress in MHBS at different loading stages corresponding at different loading stages

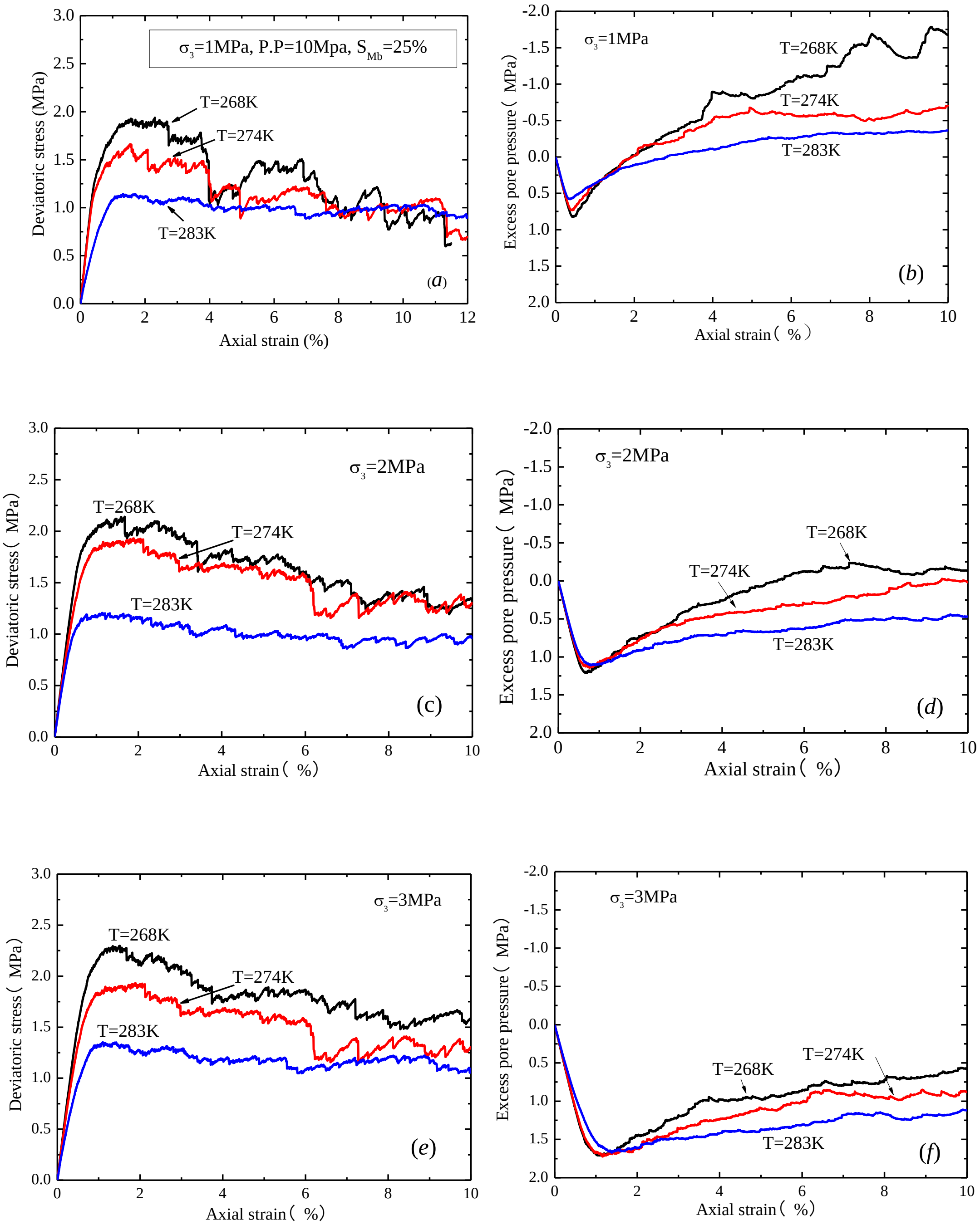

Fig. 12. Stress-strain relationships of MHBS at different temperatures and corresponding envolution of excess pore pressure under different effective pressures during loading process

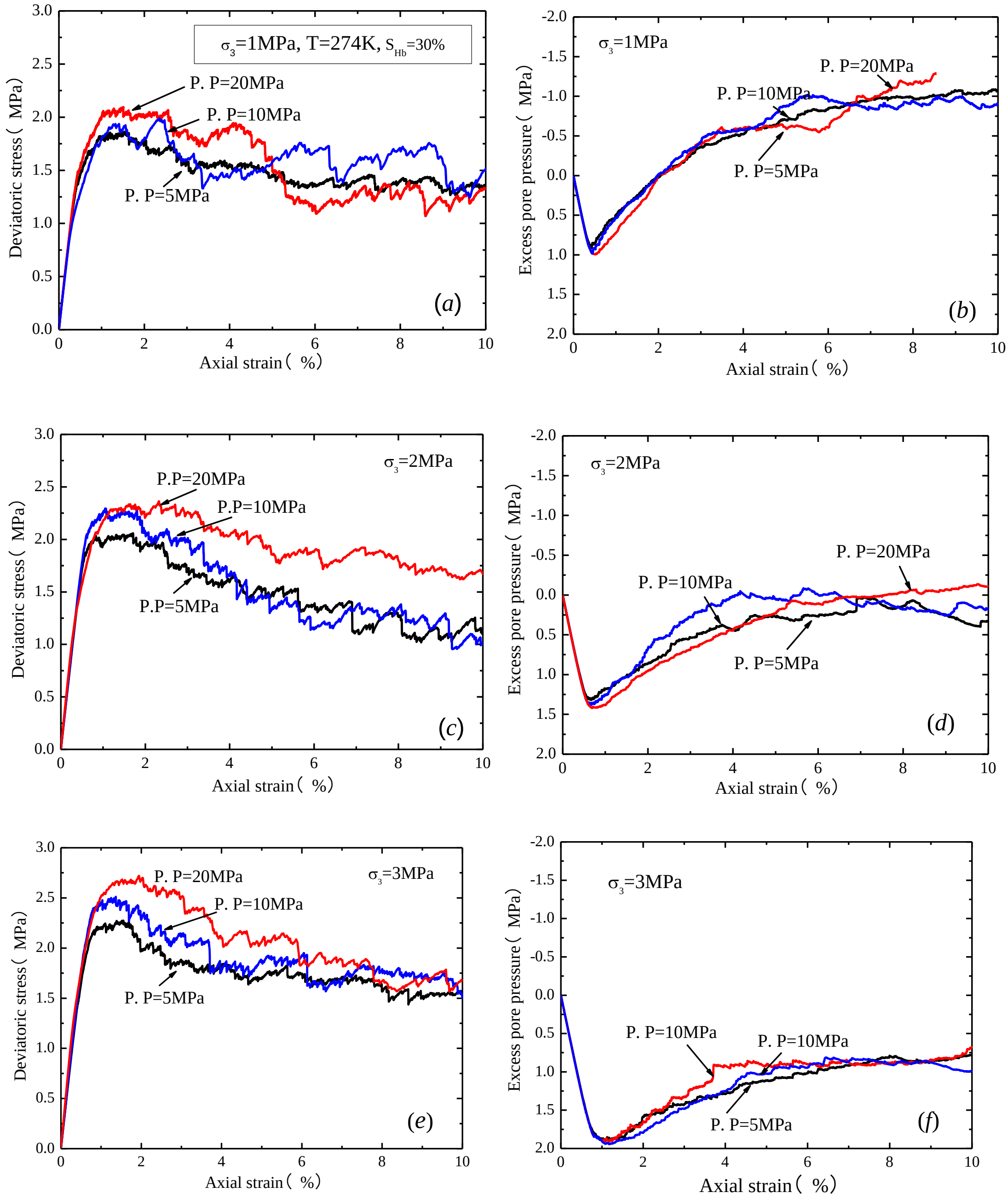

Fig. 13. Stress-strain relationships of MHBS at different pore pressure pressures and corresponding envolution of excess pore pressure during loading proces

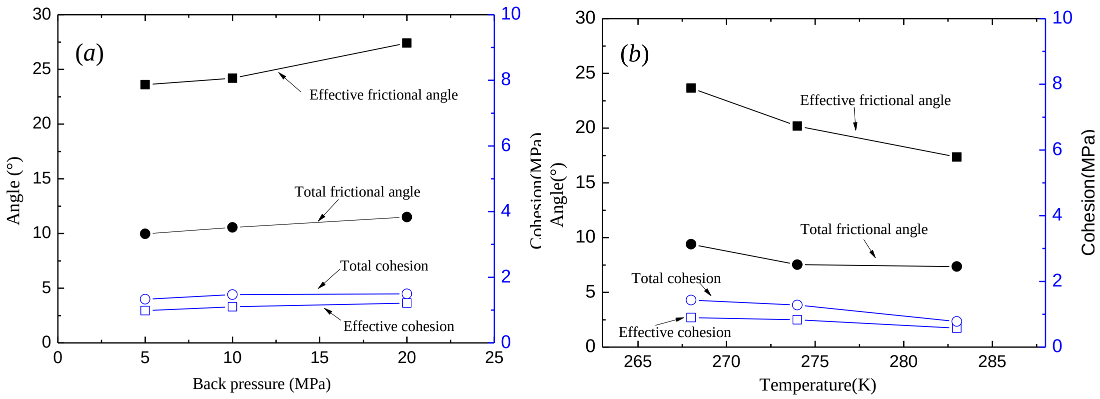

Fig. 14. Frictional angle and cohesion of MHBS with the variation of: (*a*) back pressure (*b*) temperature

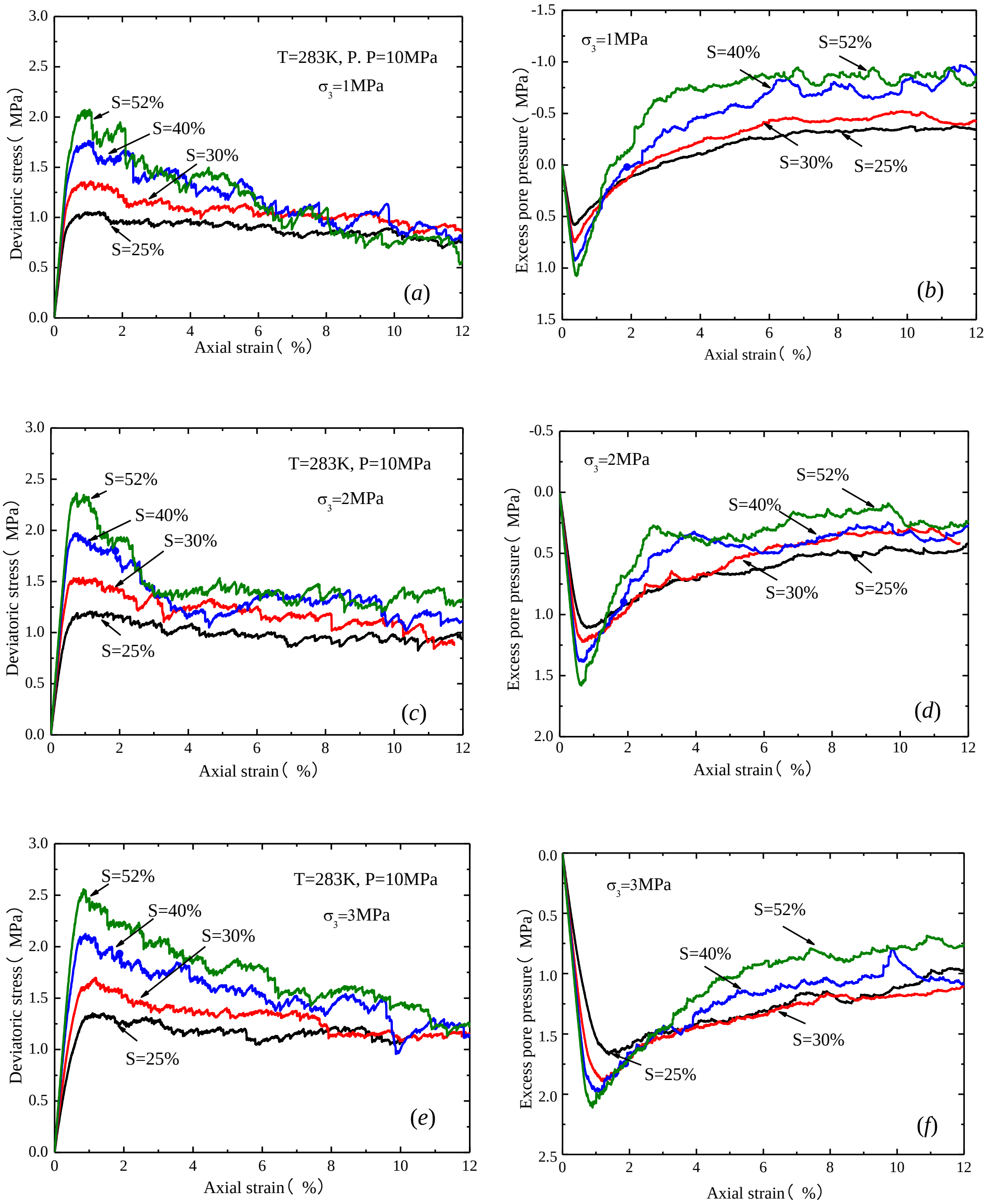

Fig. 15. Stress-strain relationships of MHBS at different saturation degrees and corresponding envolution of excess pore pressure during loading process

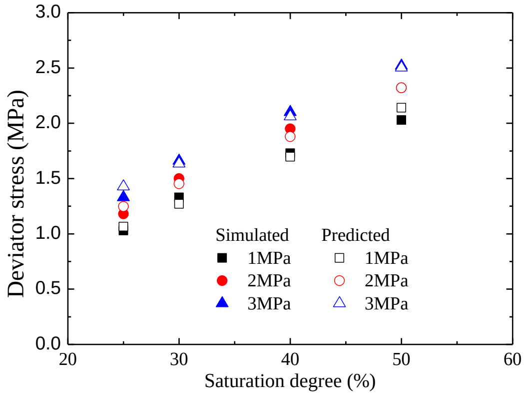

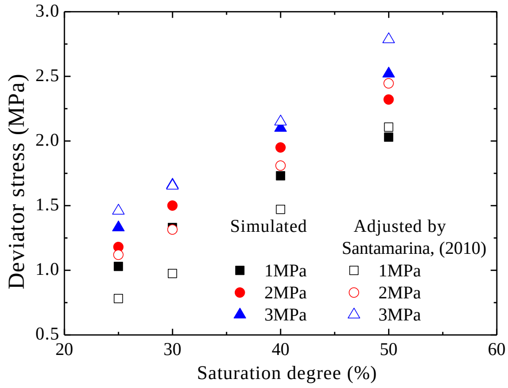

Fig. 16. Stress strain relationships with different saturation degree at different confining pressures

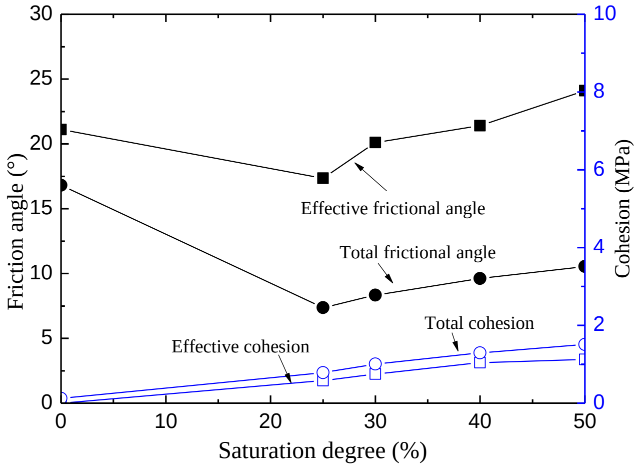

Fig. 17. Impact of saturation degree on the friction angle and cohesion

Figure captions

Fig.1. Schematic illustration of: (a) two sandy grains bonded by methane hydrate in between; and (b) contact forces between two particles

Fig. 2. Schematic illustration of a bond contact model and its mechanical response: (a) normal direction; (b) tangential direction; (c) rolling direction; (d) three-dimensional space envelope for the normal – tangential - moment strength F_n-F_s - M.

Fig. 3. Steps on coupling the motion of discrete and continuous phase (based on Favier, 2009)

Fig. 4. Comparison of the CFD-DEM prediction and the analytical solution for single particle free settling in water: (a) Particle velocity; (b) force acting on the particle at different time

Fig. 5. Relationship between settlement of the first top particles and the additional pressure

Fig. 6. Comparison of excess pore pressure between CFD-DEM numerical results and Terzaghi's theory

Fig. 7. Degree of consolidation with time factor in CFD-DEM simulation and Terzaghi's theory

Fig. 8. Schematic illustration of: (a) The numerical sample after consolidation in DEM analyses; and (b) CFD mesh (unit in mm)

Fig. 9. Particle size distribution used in CFD-DEM simulation

Fig. 10. (a) Stress-strain relationship and (b) corresponding evolution of excess pore pressure of MHBS at T=268K, P=10MPa and S_{Hb}=25% compared with clean sand under different effective confining pressure; (c) Effective and total envelopes for MHBS.

Fig. 11. Bond breakage progress in MHBS at different loading stages corresponding at different loading stages

Fig. 12. Stress-strain relationships of MHBS at different temperatures and corresponding envolution of excess pore pressure under different effective pressures during loading process

Fig. 13. Stress-strain relationships of MHBS at different pore pressure pressures and corresponding envolution of excess pore pressure during loading proces

Fig. 14. Frictional angle and cohesion of MHBS with the variation of: (a) back pressure (b) temperature

Fig. 15. Stress-strain relationships of MHBS at different saturation degrees and corresponding envolution of excess pore pressure during loading process

Fig. 16. Stress strain relationships with different saturation degree at different confining pressures

Fig. 17. Impact of saturation degree on the friction angle and cohesion

Table

Table 1. Test conditions for methane hydrate bearing sediments

NO.	***T*(K)**	***P.P*(MPa)**	**S_{Hb}(%)**
01	-	-	0
02	268	10	25
02	268	10	25
03	274	10	25
04	283	10	25
05	274	5	30
06	274	10	30
07	274	20	30
04	283	10	25
08	283	10	30
09	283	10	40
10	283	10	50

Table 2. Material parameters used in the DEM analyses

Item	Value
Density of particles	2600 kg/m^3
Normal stiffness of particles	6×10^7 N/m
Tangential stiffness of particles	4×10^7 N/m
Coefficient of friction between particles	0.5
Coefficient of rolling resistance between particles	0.5
Normal stiffness between walls and particles	6×10^7 N/m
Tangential stiffness between walls and particles	4×10^7 N/m
Coefficient of friction between walls and particles	0.0
Initial density of fluid (standard atmospheric pressure)	1000 kg/m^3
Coefficient of viscosity of fluid	0.002 Pa.s
Salinity of fluid	3.5%